

Harnessing speckle images: efficient extraction of hidden information

Weiru Fan,^{a,†,*} Xiaobin Tang,^{a,†} Xinqi Xu,^a Huizhu Hu,^b Vladislav V. Yakovlev,^c Shi-Yao Zhu,^a Da-Wei Wang,^{a,b,d,*} Delong Zhang^{a,*}

^aZhejiang Key Laboratory of Micro-Nano Quantum Chips and Quantum Control, School of Physics, and State Key Laboratory for Extreme Photonics and Instrumentation, Zhejiang University, Hangzhou, 310027, Zhejiang Province, China

^bCollege of Optical Science and Engineering, Zhejiang University, Hangzhou, 310027, Zhejiang Province, China

^cDepartment of Biomedical Engineering, Texas A&M University, College Station, 77843, TX, USA

^dHefei National Laboratory, Hefei, 230088, Anhui Province, China

Abstract. Scattering obscures information carried by waves by producing speckle patterns, posing a fundamental challenge across diverse fields, from microscopy to astronomy. While machine learning has recently shown promise in speckle analysis, existing approaches are hindered by their dependence on large, labeled datasets — a significant bottleneck in many real-world applications. Here, we introduce Speckle Unsupervised Recognition and Evaluation (SURE), a groundbreaking unsupervised learning strategy for speckle recognition that eliminates the need for labeled training data. SURE’s distinctive feature lies in its ability to extract invariant features through advanced clustering algorithms to enable direct classification of high-level information from speckle patterns without prior knowledge. We demonstrate the transformative potential of this approach in two key applications: (1) a noninvasive glucose monitoring system that accurately tracks glucose concentrations over time without extensive calibration, and (2) a high-throughput communication system using multimode fibers, achieving improved performance in dynamic environments. Additionally, we showcase SURE’s unprecedented capability to classify objects hidden behind obstacles using scattered light, further broadening its scope. This versatile approach opens new frontiers in biomedical diagnostics, quantum network decoupling, and remote sensing, unlocking a transformative new paradigm for extracting information from seemingly random optical patterns.

Keywords: scattering, unsupervised learning, speckle interpretation, pattern recognition, image sensing.

†These authors contributed equally to this work.

*Weiru Fan, E-mail: weiru_fan@zju.edu.cn; Da-Wei Wang, E-mail: dwwang@zju.edu.cn; Delong Zhang, E-mail: dlzhang@zju.edu.cn

34 **1 Introduction**

35 The complex way coherent waves interact with nonuniform materials has long been seen as a
36 major challenge in optical systems. When waves encounter such media, elastic light scattering
37 generates intricate speckle patterns with seemingly random intensity distributions^{1,2}. For many
38 applications involving coherent waves, such as optical and ultrasound imaging through turbid
39 media, speckle is often considered noise, and sophisticated signal/image processing methods are
40 applied to minimize speckles³⁻⁵. However, speckle patterns also contain important structural
41 information, and their analysis can lead to achieving super-resolution imaging^{6,7} and provide
42 texture assessment for different samples⁸. Accurate decoding of these speckle patterns might reveal
43 a wealth of information to allow for better imaging and sensing. A stunning example of utilizing
44 speckles for high-resolution spectroscopic measurements has recently been demonstrated by Cao's
45 group at Yale University⁹. Extensive computational analysis of speckles can also facilitate lensless
46 3D single-shot imaging through scattering media¹⁰.

47 One way to take an advantage of the wealth of information encoded in speckle patterns is to
48 use statistical approaches based on correlation analysis^{11,12} and transmission matrix^{13,14}. Such
49 strategies have resulted in several applications of speckle imaging for biomedical applications¹⁵.
50 However, such speckle analysis strongly depends on the sample's structure and texture due to the
51 fact that different tissues have a different size distribution of scatterers, making it difficult to
52 generalize this approach to arbitrary scattering media. Wavefront shaping is alternative resorting
53 intricate iterative algorithms and/or tremendous physical prior to retrieve information from
54 speckles¹⁶⁻¹⁹. Machine learning (ML), on the other hand, provides a powerful tool to process
55 complex data, showing promise in addressing the challenges of speckle interpretation and imaging
56 while possessing high generalizability and scalability²⁰⁻²³. To this point, computational methods
57 based on supervised learning, however, have been dominated by image reconstruction from
58 speckles which requires an extensive library of ground truth measurements which may or may not
59 be available for the system of interest. Furthermore, image sensing, which can be described in
60 terms of the position or shape or any other specific property of an object under study, does not
61 necessarily require the whole image to be reconstructed with great accuracy because it commonly
62 contains a massive amount of redundant or irrelevant information²⁴. A ground-breaking paradigm

63 of image sensing utilizes scattering as a means of encoding and then directly extract the salient
64 features to compress images into a low-dimensional space. In this framework, the optical system
65 and related algorithms do not utilize speckle patterns for imaging purposes, but search for high-
66 level information for the downstream tasks. This is conceptually similar to an approach widely
67 used in biomedical imaging in utilizing dynamic speckle information to assess blood flow²⁵.

68 In general, the concept of ‘class’ represents high-level information that is essential for
69 understanding and managing complex data, such as speckles. For instance, the proper classification
70 of speckles can be used to aid in diagnosing patients’ health conditions^{26,27}, while different classes
71 of speckles in optical communication may represent transmitted signals or data values^{28,29}. Despite
72 the overall simplification of the initial problem, the accurate speckle classification remains
73 enormously challenging when using standard image processing methods, as even a minor shift in
74 the incident wavefront can lead to substantial variations in speckle patterns. ML has been proposed
75 as a way to implement a high-performance classifier and has also demonstrated its scalability for
76 characterizing speckle patterns and for imaging from speckles^{20,30}. In one of such illustrative
77 examples, ML was successfully employed to learn the transmissive properties of scattering
78 media²⁰. However, the ultimate performance of ML significantly relies on the design of the
79 computational graph and training³¹. To perform speckle interpretation, an enormous amount of
80 labeled data is required to successfully calibrate the computational graph. Unfortunately, in most
81 situations, the ground truth is often unknown making it impossible to obtain labeled data and to
82 train; thus, a lack of sufficient ground truth for training results in limited generalization³². To
83 mitigate this problem, transfer learning and semi-supervised learning are proposed to reduce the
84 requirement of labeled data for training³³⁻³⁵. However, even a small amount of labeled data is still
85 unavailable in many practical applications, especially involving never-before-seen scattering
86 media. Therefore, there is a clear need to explore alternative approaches.

87 Here, we introduce and validate a transformative paradigm in speckle sensing through
88 Speckle Unsupervised Recognition and Evaluation (SURE), an automated clustering algorithm
89 that fundamentally shifts the paradigm on extracting information from scattered light ([Fig. 1](#)).
90 SURE represents a significant departure from conventional approaches by eliminating the need for
91 ground truth or labeled training data, instead leveraging the inherent relationships within input
92 speckles themselves. The conceptual novelty of our approach lies in a fundamental physical
93 insight: speckle patterns encode the 3D distribution of the refractive index within a system under

94 coherent light illumination. By analyzing these speckle images and comparing them across whole
95 datasets to reveal intrinsic correlations, one can extract unique structural features provided an
96 appropriate analysis framework is employed. To accomplish this challenging task, we introduce a
97 unique signal processing algorithm that bootstraps high-level features across multiple speckle
98 patterns and systematically assigns cluster labels based on predefined protocols. This enables
99 robust, unsupervised pattern recognition and characterization of complex systems. Taken together,
100 this work introduces a fundamentally new approach to optical signal processing that overcomes
101 the limitations imposed by labeled data which are traditionally used in machine learning-dominant
102 approaches. By eliminating the need for explicitly defined input–output relationships, SURE
103 enables highly generalizable, unsupervised information extraction. Although we focus on speckle
104 patterns to demonstrate the concept, the approach is broadly applicable to other complex optical
105 pattern recognition tasks.

106 In terms of instrumentation, SURE breaks with conventional paradigms by transforming stray
107 light and other complex optical signals from sources of noise into valuable information. This not
108 only enhances the capabilities of existing optical systems but also opens the door to entirely new
109 classes of applications previously considered impractical or inaccessible. We experimentally
110 validate our hypothesis that SURE redefines light scattering from being an obstacle, as
111 traditionally perceived, to becoming a powerful mechanism for encoding and extracting
112 information, fundamentally shifting how complexity is leveraged in optical signal processing. This
113 capability enables breakthrough applications such as noninvasive glucose monitoring, where the
114 algorithm successfully extracts meaningful data from dynamic speckles in flowing blood by
115 identifying time- and space-invariant patterns. The broader impact of SURE extends across
116 multiple domains of light scattering applications, from optical communications³⁶ to remote
117 sensing³⁷ and tomography³⁸. In a striking demonstration, we achieved a two-orders-of-magnitude
118 increase in bandwidth through optical communication within a dynamic multimode fiber (MMF),
119 showcasing SURE’s ability to handle complex, time-varying scattering environments.
120 Collectively, these results demonstrate that SURE is capable of revealing underlying, previously
121 inaccessible information embedded within speckle patterns which is far beyond superficial
122 morphological features. As a versatile and scalable methodology, SURE holds disruptive potential
123 to accelerate scientific discovery and drive innovation across both academic research and industrial
124 applications.

125 Comparative analysis reveals SURE’s unique advantages over existing speckle processing
 126 methods (Table 1). While traditional approaches often sacrifice capability in one area to excel in
 127 another, SURE maintains high performance across multiple metrics - from single-shot capability
 128 to complex object classification - while requiring no labeled training data. This comprehensive
 129 performance profile positions SURE as a versatile solution for emerging applications ranging from
 130 optical image processing to secure communication systems. This work represents a fundamental
 131 advancement in speckle-based sensing and imaging through three key innovations: the
 132 development of a pioneering unsupervised learning framework that eliminates dependency on
 133 labeled data; the creation of a novel clustering algorithm capable of extracting invariant features
 134 from apparently random speckle patterns; and the validation of a unified framework demonstrating
 135 unprecedented versatility across various scattering conditions. These advances collectively
 136 establish a new paradigm for harnessing the information-rich nature of speckle patterns, opening
 137 new possibilities in fields from biomedical imaging to quantum communications.

138 **Table 1** Comparison between different speckle processing modalities for hidden information extraction.

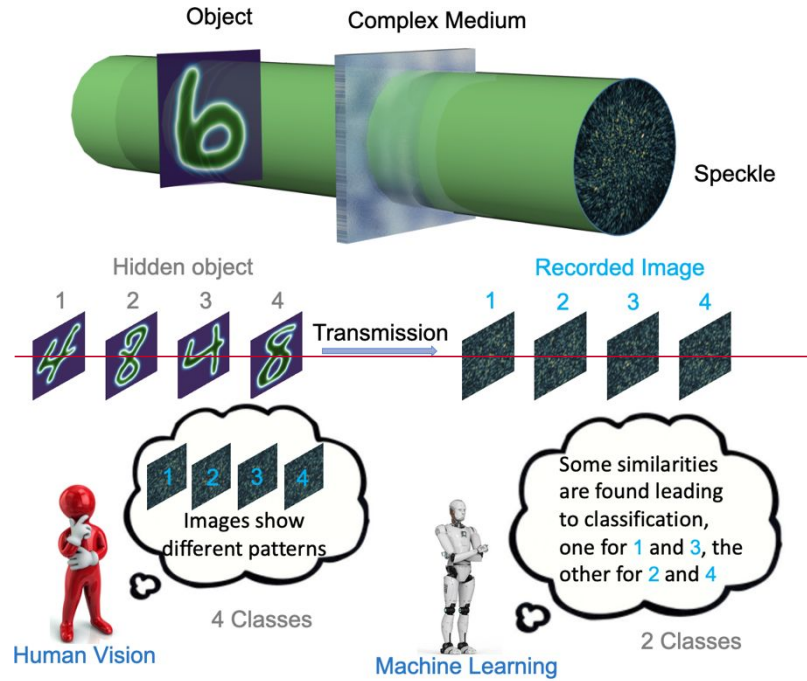
	Single-shot capability	Dynamic Scattering	Phase retrieval- free	Multiple scattering	Complex object	Classification	Prior- free	Labeled data free	Ref.
Digital filter	✓	✓	✓	N/A	N/A	N/A	N/A	✓	[5]
Texture analysis	✓	✓	✓	N/A	✓	✓	N/A	N/A	[8]
Speckle contrast	N/A	✓	✓	N/A	N/A	N/A	N/A	✓	[25]
Transmission matrix	✓	N/A	N/A	✓	✓	N/A	✓	N/A	[13,14,28]
Speckle correlation	✓	✓	N/A	✓	N/A	N/A	N/A	✓	[11,12]
Machine learning	✓	✓	✓	✓	✓	✓	✓	N/A	[20-23]
SURE	✓	✓	✓	✓	✓	✓	✓	✓	This work

139

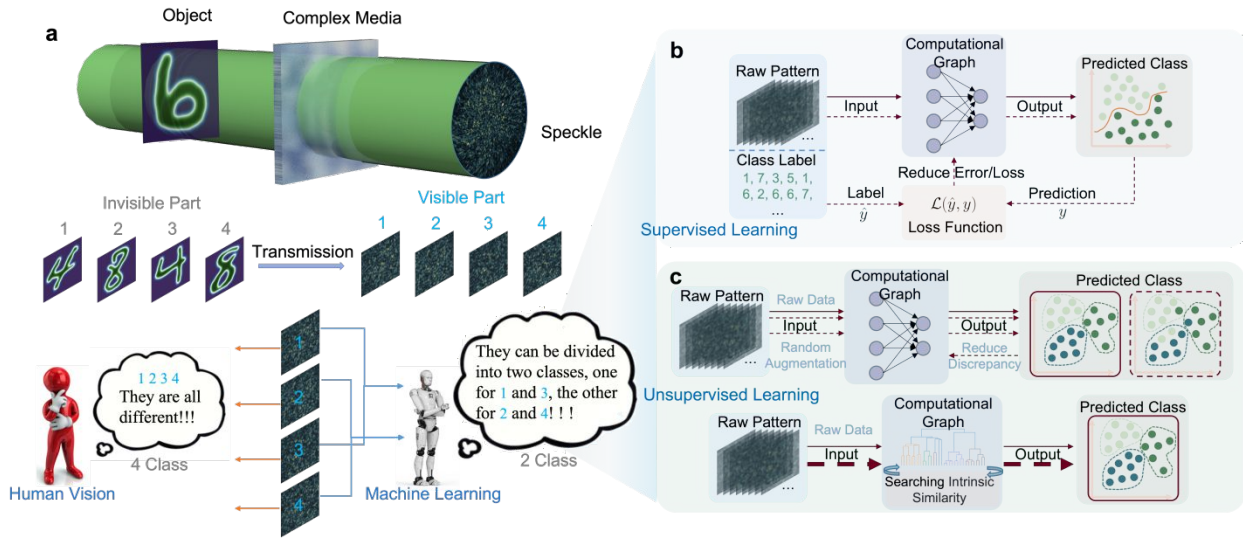
140 **2 Results**

141 SURE utilizes the automated clustering within an unsupervised learning framework to reveal
 142 internal correlations hidden in these seemingly irrelevant speckles. Remarkably, it extracts
 143 information without requiring extensive ground truth or labels that are typically unavailable in
 144 speckle interpretation (Fig. 1). SURE contains two major elements: clustering the speckles without
 145 any labeled data and assigning corresponding semantic labels to the resultant clustered groups (one
 146 labeled sample per class). The goal of clustering is to discern the high-level correlations (label of
 147 class) within speckles, independent of their specific meanings. The implementation of

148 conventional image clustering is according to the salient structural features from the images, e.g.,
 149 clustering the handwritten digits, which is also realizable for human vision. However, the input
 150 and its corresponding speckles in our case are uncorrelated in spatial structures, such that SURE
 151 seeks invariant information to achieve clustering. To achieve this, computational graphs with a
 152 self-learning framework are vital to grasp the invariant information facilitating the automated
 153 clustering.



154



155

156 **Fig. 1** The overall concept of speckle clustering for image recognition and the data workflow. (a) Overview of speckle
 157 interpretation. Light carrying object information passes through random media yielding corresponding speckles, where

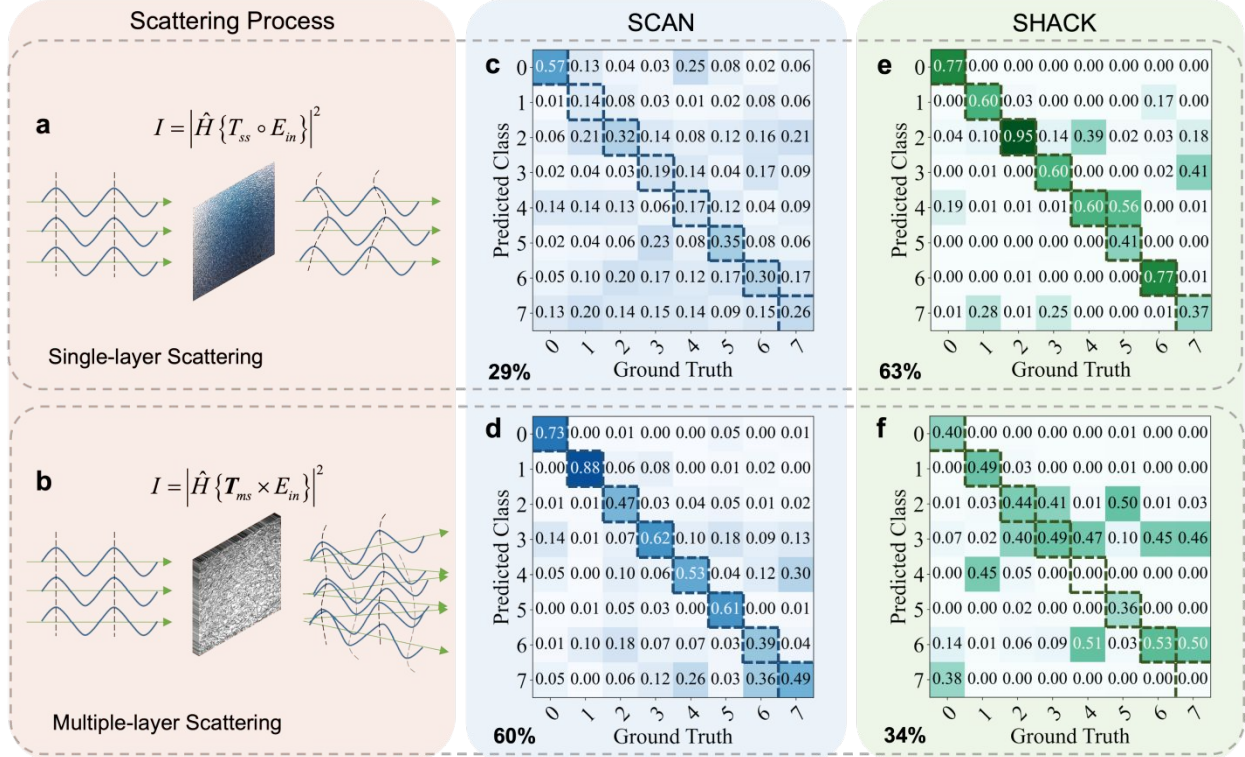
158 a slight perturbation in the wavefront leads to significant speckle decorrelation. These speckles lack salient structural
159 features and exhibit an irregular intensity distribution, such that the original information is scrambled and concealed.
160 Without prior knowledge, it is difficult for human vision to extract the critical information of speckles, while machine
161 learning can accurately extract the intrinsic features of speckles and correctly classify them. (b) and (c) Workflow of
162 supervised and unsupervised learning-based machine learning, respectively. The supervised learning methods utilize
163 the labelled data and explicitly calculate the error by the loss function to optimize parameters of computational graph.
164 The unsupervised learning approaches calibrate the computational graph by contrastively learning or searching intrinsic
165 similarity without labels. The solid and dashed red line represent the dataflow of the prediction and training,
166 respectively.

167 The efficiency of computational graphs for extracting invariant information is discrepant
168 under different physical properties of scattering media³⁹. Therefore, it is crucial to design
169 appropriate computational graphs to implement SURE. Generally, linear scattering media can be
170 categorized into single/thin and multiple/thick scattering layers¹. In single-layer scattering, light
171 passing through the media, e.g., ground glass, water mist and thin biological tissue, merely
172 undergoes a random phase shift at different spatial positions but its direction remains unchanged
173 (Fig. 2(a)). Consequently, the original information carried by the beam is still locally embedded in
174 the same positions/pixels before and after the media, defined as local embeddedness. This process
175 can be described by a Hadamard product between input field E_{in} and the matrix T_{ss} with the same
176 number of complex elements. In contrast, with multiple-layer scattering media, e.g., egg
177 membrane, plastered wall and MMF, the change simultaneously appears in both random phase
178 shift and propagation direction (Fig. 2(b)). The global information is carried throughout in this
179 case because each speckle grain arises from a coherent superposition of all elements on the incident
180 light, defined as global embeddedness. It can be described by a matrix-vector multiplication
181 between input field E_{in} and complex matrix T_{ms} with $m \times n$, where m is the number of pixels of
182 speckle in the detector and n is the number of elements of input field.

183 We meticulously design computational graphs for each aforementioned category to
184 accommodate SURE and enhance the performance of speckle image sensing. These graphs are
185 termed as speckle clustering aware network (SCAN) and speckle hierarchical agglomeration
186 clustering knack (SHACK), respectively (Supplement Material and Fig. S1 for details). The former
187 is based on a deep neural network which is suitable for processing speckles with global
188 embeddedness, because it has the capability to perceive and capture the high-level correlation
189 among speckles. The SHACK employs a binary tree to propel the speckle image sensing with local
190 embeddedness. Similar to traditional learning-based methods, SCAN and SHACK convert the

191 speckle clustering into an optimization question to process complex data. The optimization targets
192 are to iteratively minimize the objective function. SCAN's objective function has the form of
193 $\operatorname{argmin}\left\{\sum_i L(F_{NN}(x_i), F_{NN}(T(x_i)))\right\}$ and SHACK's is the $\operatorname{argmin}\left\{\sum_{ij} d(x_i, x_j)\right\}$, where x_i is the i -th
194 speckle pattern, the $F_{NN}(\cdot)$ represents neural network for SCAN, $T(\cdot)$ is a random transformation
195 of the original speckle pattern, $L(\cdot)$ is the loss function for SCAN, $d(x_i, x_j)$ is the distance between
196 x_i and x_j , and $\operatorname{argmin}\{\cdot\}$ is the value of the variable that minimizes the following expression. See
197 Appendix and Supplement Material for principles and details.

198 To demonstrate the performance of these two frameworks, we implemented the automatic
199 clustering for speckle image sensing from the single- and multiple-layer scattering media (see
200 Supplement Material Fig. S2 for experimental setup). The quantitative results are shown in Fig.
201 2(c)-(f) by confusion matrices. These results indicate that SHACK has a higher accuracy for
202 processing single-layer scattering, where the results are dominated by the diagonal terms of the
203 confusion matrix, however, SCAN involves all matrix elements. Complementarily, SCAN
204 effectively handles the speckle generated from the multiple-layer scattering, with its results
205 focusing on the diagonal terms of the confusion matrix, while SHACK outputs a series of random
206 values. These frameworks collectively characterize the performance of speckle interpretation
207 across diverse scenarios by SURE. To further validate the universality of SURE, the clustering is
208 accomplished with different number of classes (tasks with 2, 4 and 8 classes), and the results are
209 consistent with the previous analysis (shown in Supplement Material Fig. S3).



210

211 **Fig. 2** Speckle image clustering analysis. (a, b) Wavefront evolution diagrams for single- and multiple- layer
 212 scattering, respectively, where \hat{H} represents the free-space light propagation operator. (c, d) Clustering results
 213 obtained using SCAN algorithm for speckles generated by single-layer and multiple-layer scattering, respectively. (e,
 214 f) show SHACK's clustering results with speckles generated by single-layer and multiple-layer scattering,
 215 respectively. In (c-f), dashed boxes indicate true positives, and the accuracy values are displayed in the lower left
 216 corner of each subgraph. The Hadamard product is denoted by \square , while $|\cdot|$ represents the amplitude of the electric
 217 field. Wavefront phase modulation was performed using images from the MNIST dataset, where different images of
 218 the same digit correspond to the same classification class.

219

220

221

222

223

224

225

226

227

It is worth pointing out that SCAN and SHACK can have comparable performance in speckle
 image sensing when more computing resources are invested to improve the generality of SURE,
 such that the deliberately selecting either of them is unnecessary. This allows us to bolster the
 execution of speckle image sensing by expanding the computational graphs. For instance, an
 improved performance of SCAN in single layer scattering can be achieved by increasing the
 parameter scale, e.g., the channel number of the convolutional layer and the depth of the network.
 Additionally, the combination of data dimension reduction methods and SHACK can also be used
 to enhance the extraction of abstract invariant information from speckles. Furthermore, our results
 indicate an accuracy surpassing 50% for categorization tasks with 8 classes, compared to a baseline

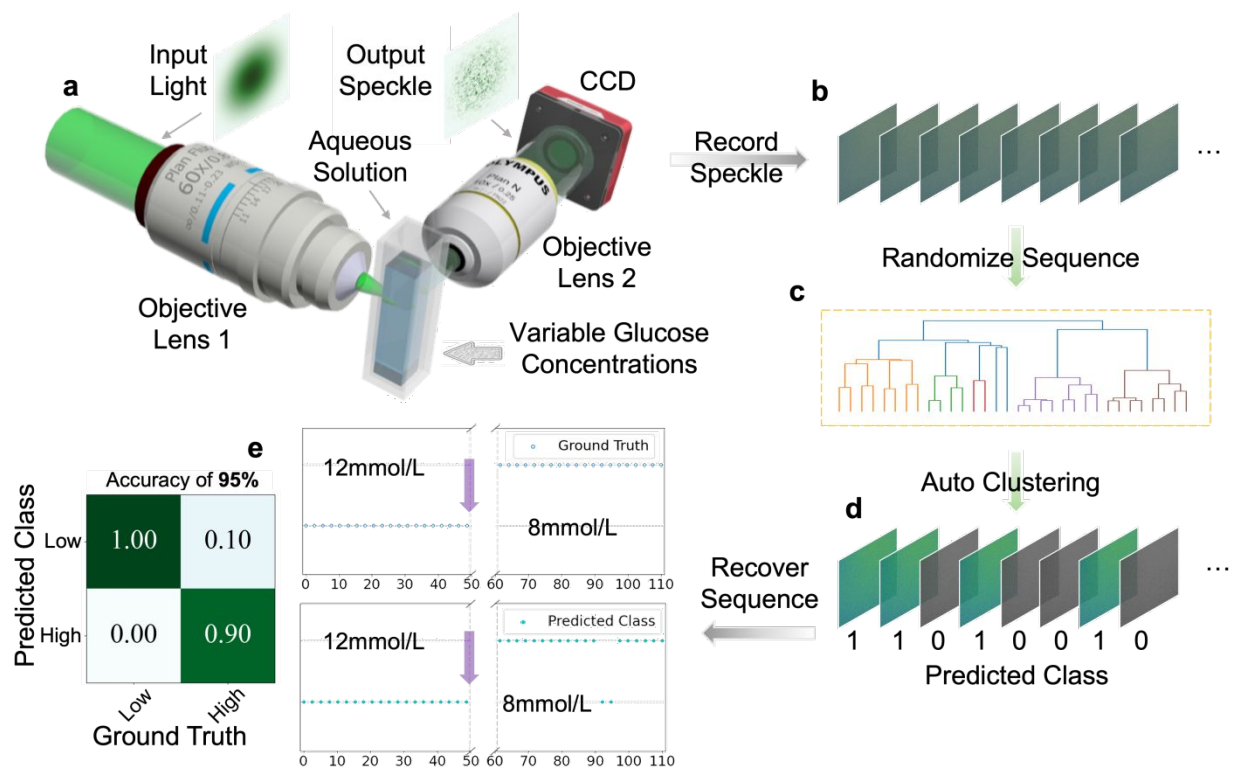
228 of 12.5% for random guessing (see Fig. 2). This means that this accuracy can be further increased
229 by involving ensemble learning with the boosting techniques^{40,41}.

230 Once the speckle image sensing is achieved by SURE, various applications without labeled
231 data can be developed by embedding SURE into their corresponding pipelines. As a proof-of-
232 concept demonstration, we propose a SURE-based noninvasive glucose monitoring where data
233 labels are not routinely available due to the structural anisotropy and variability of underlying
234 tissues. In clinical practice, invasive blood collection remains the mainstream method for diabetes
235 management thanks to its high precision, convenience and low cost⁴². However, it causes
236 secondary injuries to patients, and also increases infection risks. Remote optical methods for
237 glucose detection are promising in biomedical applications because of their noninvasiveness and
238 selectivity^{43,44}. Amidst the current optical noninvasive blood glucose testing, one of the key
239 challenges is that skin tissue hinders light penetration.

240 When the probe light passes through the biological tissues^{45,46}, the strong scattering leads to
241 signals hiding in the complex speckle background, and thus poses a challenge for glucose
242 monitoring^{47,48}. To address this issue, the combination of ML and optical apparatuses enables the
243 extraction of the glucose signal from speckle backgrounds with a high signal-to-noise ratio^{497,5048}.
244 However, a large number of labeled samples is needed to train an ML model for extracting relevant
245 features to achieve anomaly detection and diagnosis due to the intricacy and enormity of glucose
246 monitoring⁴⁹⁵¹⁻⁵³. Due to the individual-specific nature of these features, noninvasive blood
247 glucose monitoring still requires multiple invasive blood collections daily to build a training
248 dataset for an individual patient, increasing the risk of repeated injuries and infections⁵⁴⁹.
249 Moreover, a tiny shift in the probe position can completely invalidate these labels (see Supplement
250 Material Fig. S4), making it difficult to calibrate the ML model.

251 Towards this goal, we experimentally validated the SURE-based noninvasive glucose
252 monitoring in a right-angle scattering configuration, in which a biological membrane was
253 introduced to mimic skin tissues (Fig. 3(a)). A series of speckle patterns were collected from the
254 aqueous solutions for a fixed glucose concentration. We repeated the same procedure for different
255 glucose concentrations, and these recorded speckle patterns were randomly shuffled in their
256 sequence and fed into the computational graph (SCAN/SHACK) (Fig. 3(b) and (c)). The
257 computational graph automatically sought the high-level features of speckles to achieve the
258 clustering (Fig. 3(d)). After that, the true concentrations were assigned to different classes

259 depending on the tagged speckles, where an additional one-time invasive collection was
 260 implemented to label one speckle within each class. Note that the speckles exhibit minute random
 261 variations even in a concentration-uniform solution, due to local concentration fluctuations of the
 262 solution⁵⁵¹⁻⁵⁷³. Such a random effect (like blood flow) leads to time-dependent speckles,
 263 complicating concentration classification in the actual scenario. Strikingly, since SURE is based
 264 on the invariant information, our strategy was found to be immune to speckle shifts arising from
 265 local fluctuations.

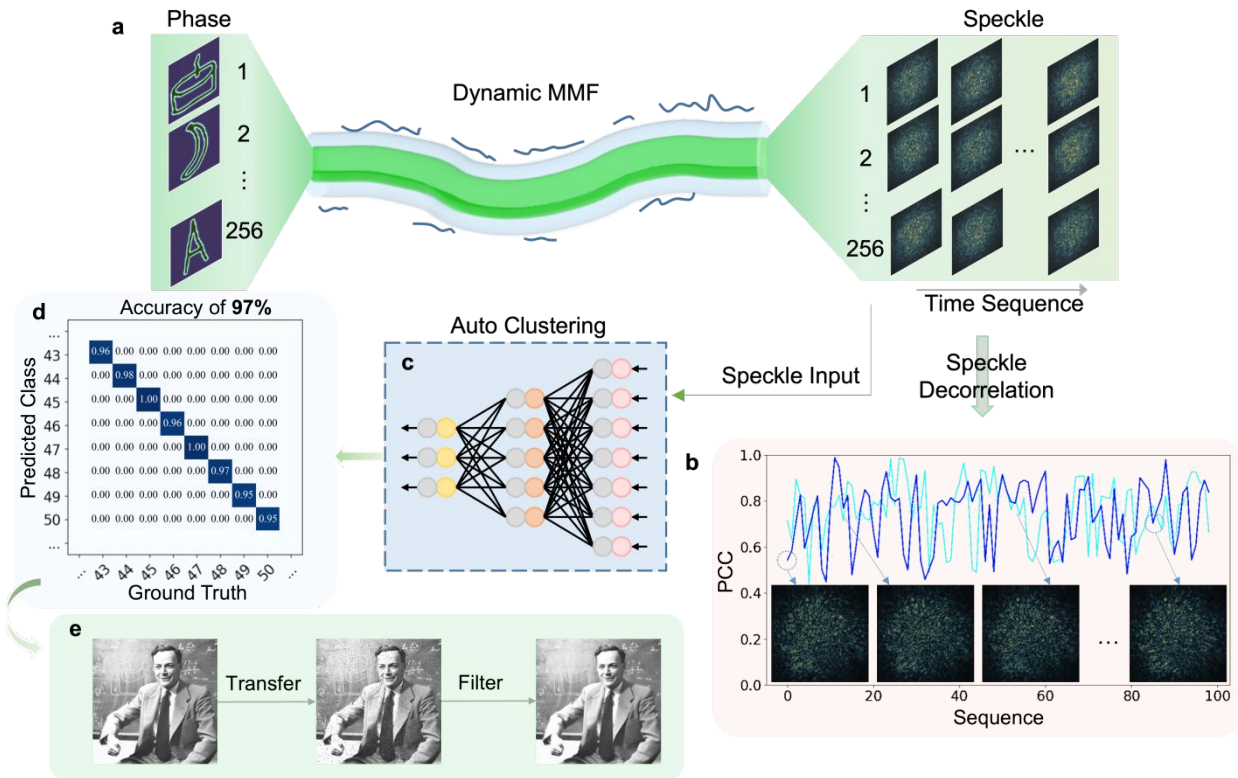


266
 267 **Fig. 3** Speckle-based noninvasive glucose monitoring. (a) Schematic of an experimental setup. A laser beam is focused
 268 on the sample using a 50× objective lens (NA = 0.6), and the speckle patterns are collected using a 10× objective lens
 269 (NA = 0.3) at a 90° angle. (b) Speckle images are collected and then randomly shuffled. (c) Image clustering is
 270 performed using SHACK algorithm. (d) Predicted classes are assigned. (e) Quantitative analysis results obtained from
 271 20 datasets for each glucose concentration. The hollow and solid dots represent the ground truth and the predicted
 272 results, respectively. To emulate the optical scattering properties of biological tissues, the rear surface of the sample
 273 cuvette was covered with an eggshell membrane, and the remaining three surfaces were covered with adhesive tape
 274 (actual sample configuration shown in Supplement Material Fig. S6).

275 As a result, we demonstrated 95% accuracy in identifying the classes of concentration from
 276 the time-dependent speckles (Fig. 3(e)). Here, two classes of concentration were used for proof-
 277 of-concept demonstration, i.e., 8 mmol/L and 12 mmol/L which are approximately within the

278 blood glucose ranges of healthy people and diabetes patients. The binary classification is sufficient
279 to determine whether the blood sugar is abnormal. In practical applications, more levels of glucose
280 concentration can be involved by adjusting the preset class numbers, e.g., 8 classes (The results
281 are shown in Supplement Material Fig. S5). In addition, one concern in data collection is that the
282 speckle patterns exhibit a time correlation, i.e., speckles that are closer in the time domain tend to
283 have a more similar spatial distribution. Therefore, we need to exclude the possibility that the
284 clustering merely reflects such time correlation. To realize this, we increased the time interval of
285 data acquisition and performed a control experiment in which the glucose solution was replaced
286 with clear water while others remained unchanged. The results of the control group revealed an
287 accuracy of 60%, which is close to the random accuracy baseline (50%). Thus, the clustering
288 results can be attributed to different concentrations rather than time correlation (see Supplement
289 Material Fig. S6 for additional data and comparisons). It is also worth noting that other components
290 in the body can also be detected and monitored following a similar procedure. If the biological
291 variability is not abrupt, the trained computational graph of SURE is robust because it gets rid of
292 the labelled data, enabling fine-tuning and evolving itself with real-time data. Otherwise, we must
293 retrain using the data from the new situation.

294 To further demonstrate the versatility, SURE was deployed into optical communication to
295 achieve high-throughput information transport under dynamic multimode fiber (MMF). Optical
296 fibers serve as the backbone of telecommunication which are ubiquitous in modern society⁵⁸⁴.
297 Over the past decades, the data-carrying capacity of fibers has surged by several orders of
298 magnitude through various multiplexing techniques, in which the optical power injected into fibers
299 is growing higher and higher⁵⁹⁵. However, the higher optical power used, the stronger nonlinear
300 effect produced by optical fibers^{595,6056}, severely constraining the continued increase in bandwidth
301 of optical communication. As a solution, we propose a novel scheme to improve the bandwidth,
302 where the wavefront phase is used to encode information while SURE is employed to decode the
303 signal. In this strategy, the different spatial phase distributions can generate significantly different
304 speckle patterns²⁰, such that the mutually orthogonal modulations of input wavefront are
305 unnecessary. Therefore, leveraging the wavefront phase can be conducive to high-bandwidth
306 information transport.



307
 308 **Fig. 4** High-throughput dynamic information transmission through multimode fiber. (a) A schematic of the
 309 experimental approach. Phase images were created on the input of the MMF, and corresponding speckle images were
 310 collected on the output. For any given input wavefront of light, a time-dependent disturbance of the MMF results in
 311 significant temporal variations of speckle patterns. (b) Temporal correlation analysis of speckle images generated from
 312 identical phase images at different time points. Light blue and dark blue lines represent correlation profiles for two
 313 distinct modulation patterns belonging to different classes. (c) Compute graph (SCAN) used for clustering time-
 314 dependent speckles. Each speckle pattern serves as input, with the corresponding predicted class as output. Colored
 315 circles denote input, output, and hidden neurons, while grey circles represent activation functions (detailed architecture
 316 provided in Appendix). (d) Confusion matrix demonstrating clustering performance for 10 randomly selected classes
 317 from the complete set of 256 encoded phase maps. The SCAN algorithm achieved 97% accuracy across all 256 classes.
 318 (e) Experimental demonstration of image transmission using pixel-by-pixel encoding strategy. A median filter was
 319 applied to remove impulse noise. The accuracy difference between SHACK (89%) and SCAN (97%) algorithms was
 320 8%. Image acquisition time was 300 ms per frame, with random time intervals between successive speckle acquisitions
 321 for identical input phases. Additional data are presented in Supplement Material Figs. S7 and S8.

322 In long-distant communication, a confronting challenge arises from multiple sources, e.g.,
 323 temperature variance and mechanical vibrations, causing instability for MMF and hence resulting
 324 in alterations to the output speckles with the identical input (Fig. 4(a) and (b)). Under this
 325 condition, only a limited number of labeled cases of this random process can be obtained, making
 326 supervised learning with labeled data impractical (Supplement Material Fig. S4 as an example).

327 Instead, our SURE overcomes this limitation and is capable of handling random dynamic
328 scattering. To mimic turbulence/disturbance, we imposed random motion on the MMF during the
329 optical communication. In the procedure of transport, the wavefront phases were firstly one-by-
330 one transmitted according to the allocated sequence, and the numerical orders and the
331 corresponding speckles were used as a secret key or protocol to decode speckles and assign values.
332 Thereafter, based on this protocol (the numerical orders of speckles in here), the original data was
333 encoded and transmitted to yield the corresponding speckles. These speckles and those in the
334 protocol were mixed and fed into SCAN/SHACK to perform the clustering and assign values to
335 the clustering group according to the speckles in protocol (Fig. 4(c)). This process completed the
336 data transport using the dynamic MMF. The quantitative results are shown by the confusion matrix
337 with the accuracy of 97% (Fig. 4(d)). This result indicates that SURE can effectively uncover the
338 invariant features within dynamic speckles for clustering, enabling high-precision information
339 transport.

340 To further demonstrate the effectiveness of SURE in optical communication, which often
341 involves image transmission, we present an example featuring a photograph of Richard Feynman,
342 with the corresponding results shown in Fig. 4(e). Specifically, a series of phase maps were
343 arbitrarily chosen and numbered in ascending order as the pixel/data values. Similar to the previous
344 strategy, the speckles were acquired at the output end of the MMF and then mixed with the
345 previous speckles in protocol to cluster and assign pixel values. In parallel with current
346 multiplexing techniques, we conducted a random intensity attenuation to each recorded speckle to
347 simulate the coexisting case of intensity and phase encoding. The result of the image transport
348 exhibited high fidelity except for several anomalous pixels. These anomalies are characterized by
349 impulse noise which is tractable by the median filter (Fig. 4(e)). This indicates that the SURE-
350 based technique can effectively implement MMF-based optical communication and perform
351 speckle sensing under dynamic scattering. It is highly scalable in optical communication because
352 it overcomes the disturbance in random environments. Unless the environmental changes are
353 extremely drastic, causing the speckle to be completely decorrelation. In this case, the trained
354 parameters will be invalid. In addition to optical communication Moreover, this scheme may also
355 be extended to medical endoscopic imaging with a single MMF via spot-scanning.

356 **3 Discussion**

357 The SURE methodology provides a conceptual framework for speckle image sensing by
358 extracting abstract, invariant features from complex and noisy speckle backgrounds. Taking
359 advantage of unsupervised learning, SURE, as demonstrated in numerous examples shown above,
360 eliminates the extensive labeled dataset for training, and effectively handles the speckle
361 classification under static and dynamic environments regardless of the amount of scattering. As
362 demonstrated in two applications, SURE correctly classifies speckles associated with different
363 glucose concentrations and distinguishes images being transmitted through MMF, thus achieving
364 noninvasive glucose monitoring and enabling a high-throughput optical communication.
365 Compared with previous methods, SURE-based glucose monitoring discards the cumbersome
366 measuring apparatus and intricate algorithm, substantially simplifying the diagnosis procedure and
367 holding promise for miniaturized and portable noninvasive glucose monitors. In optical
368 communications, SURE is proven to sort the speckle data under dynamic scattering, significantly
369 improving the noise resilience and throughput of MMF-based information transport. Note that a
370 drastic environmental change could result in significant cross-correlation in speckle patterns,
371 potentially compromising the invariance properties crucial to our technique. This may be
372 addressed by integrating physical prior knowledge to constrain feature extraction and
373 implementing ensemble learning approaches to enhance speckle clustering. We also introduce the
374 mutual information to proof the effectiveness of SURE see Appendix.

375 It is important to emphasize that SURE is not confined to specific applications, but rather
376 serves as a universal solution for diverse challenges where specific information extraction from
377 complex patterns is necessary. For example, it can be used for defect detection on chips, encryption
378 and decryption of optical information, and allow signal and image recognition with single/low
379 photon illumination, i.e., it can be potentially extended to quantum imaging and biological
380 imaging, where optical damage to fragile biological samples needs to be avoided. Here, we also
381 experimentally demonstrate the classification of dynamic hidden objects in the non-line-of-sight
382 (NLOS) region, where the effective photon number is extremely low and the precise modeling is
383 impossible^{61,57}, such that the extraction of speckles-hidden information is extremely challenging.
384 Our SURE efficiently harnesses weak secondary scattered photons superimposed on strong first
385 backscattered photons to uncover dynamic hidden objects without any labels (results and setup

386 shown in Supplement Material Fig. S9 and S10, respectively), an achievement unprecedented in
 387 previous studies.

388 **Table 2** Quantitative comparison between different machine learning algorithms for speckle
 389 classification/clustering.

Tasks Methods	2-classes		4-classes		8-classes	
	MS	SS	MS	SS	MS	SS
SCAN (w/o)	0.98	0.99	0.81	0.49	0.61	0.29
SCAN (w/)	0.58	0.58	0.25	0.25	0.12	0.12
ResNet-50 (w/)	0.99	0.98	0.93	0.91	0.82	0.81
FCN (w/)	0.52	0.52	0.27	0.27	0.13	0.13
SHACK (w/o)	0.72	0.99	0.39	0.92	0.31	0.63
K-means (w/o)	0.73	0.99	0.49	0.57	0.26	0.38
DBSCAN (w/o)	0.52	0.52	0.27	0.27	0.13	0.13
MeanShift (w/o)	0.52	0.52	0.27	0.27	0.13	0.13

390 Note: w/ and w/o represent training with and without labels, respectively. The digital numbers are of accuracy.

391
 392 To quantitatively demonstrate the outstanding performance of SURE, we conduct a series of
 393 comparative studies with respect to existing methods and provide benchmark results (see Table 2).
 394 Within the deep learning framework, we first compared SCAN with unsupervised and supervised
 395 learning. The unsupervised version can perform speckle classification/clustering, but the
 396 supervised version experiences mode collapse (where all predicted results converge to a single
 397 class). This is likely due to the fact that SURE has an oversimplified architecture, causing a
 398 dilemma in capturing adequate relevant features through supervised learning. In contrast,
 399 unsupervised learning attempts to exploit invariant features to bolster optimization, thereby
 400 avoiding it. Similarly, the fully connected networks (FCN) with a five-layer architecture without
 401 normalized layer also undergoes mode collapse, however, the meticulous and sophisticated
 402 ResNet-50 can achieve high classification accuracy by supervised learning. Strikingly, the ResNet-
 403 50 and FCN still incur mode collapse when training by the same unsupervised learning with SCAN
 404 due to overcomplicated or inappropriate architectures. For SHACK, we compare it with three other
 405 widely used ML clustering algorithms. Here, DBSCAN and MeanShift also suffer from mode
 406 collapse. Although K-means can achieve clustering, its performance is worse than that of our
 407 SHACK, especially in multi-classification tasks. These results collectively emphasize the
 408 advantages and unparalleled performance of SURE.

Table 2 Quantitative comparison between different machine learning algorithms for speckle classification/clustering.

Tasks Methods	2-classes		4-classes		8-classes	
	MS	SS	MS	SS	MS	SS
SCAN (w/o)	0.98	0.99	0.81	0.49	0.61	0.29
SCAN (w/)	0.58	0.58	0.25	0.25	0.12	0.12
ResNet-50 (w/)	0.99	0.98	0.93	0.91	0.82	0.81
FCN (w/)	0.52	0.52	0.27	0.27	0.13	0.13
SHACK (w/o)	0.72	0.99	0.39	0.92	0.31	0.63
K-means (w/o)	0.73	0.99	0.49	0.57	0.26	0.38
DBSCAN (w/o)	0.52	0.52	0.27	0.27	0.13	0.13
MeanShift (w/o)	0.52	0.52	0.27	0.27	0.13	0.13

Note: w/ and w/o represent training with and without labels, respectively.

To implement SURE, SCAN/SHACK employ a contrastive learning strategy to capture the context of speckle. This usually requires data with alignment and uniformity to ensure grasping salient features among similar instances and discriminating the different instances⁶²⁵⁸. These can be boosted by imposing physical constraints and preprocessing speckle patterns. The former can be satisfied by only setting one factor needed for observation to change speckle while ensuring the others remain unchanged or uniformly varied. The latter is achieved by introducing external physical priors or resorting to the state-of-the-art pretrained models. Furthermore, designing the positive and negative samples is a practical approach to facilitate SURE⁶³⁵⁹. It is also worth discussing SURE’s two steps of clustering and label assignment. In the first step, although the clustering method is tailored for tasks involving discrete objects, auto-encoding models can be introduced to handle tasks with continuous variables. In the second step, SURE needs to integrate with existing methods or well-designed protocols to assign meaningful labels to cluster groups for specific downstream tasks. Moreover, we point out that SURE needs to select an appropriate framework (SCAN/SHACK) according to specific tasks, due to the limitations of computational resources. With ongoing advancements in both software and hardware, SURE is expected to adeptly address image sensing and speckle interpretation challenges generating new far-reaching applications.

4 Conclusion

In conclusion, we proposed, designed, experimentally demonstrated, and validated a new paradigm in speckle sensing, namely speckle unsupervised recognition and evaluation (SURE), which is

433 based on acquiring speckle patterns and utilizing an unsupervised learning algorithm to reveal
434 invisible information from speckle patterns. This approach changes the paradigm of speckle image
435 analysis since it allows to extract invariant features of what appears to look like a pure random
436 image. Importantly, we demonstrate that SURE can faithfully cluster the speckle corresponding to
437 the same class of input field, regardless of whether there is single-layer scattering or multiple-layer
438 scattering. By integrating SURE into speckle interpretation tasks, we showcase its versatility across
439 critical applications, including noninvasive glucose monitoring and harsh-condition MMF-based
440 communication. The development of SURE provides a new pathway for comprehending complex
441 optical signals and images, e.g., classify objects hidden behind obstacles using scattered light for
442 our example, with the potential to advance numerous areas in modern photonics. Its impact extends
443 across various scientific and technological fields, from deep-tissue imaging and autonomous
444 driving to remote sensing and quantum imaging.

445 **5 Appendix: Materials and Methods**

446 *5.1 Experimental Details*

447 *Experimental setup:* As shown in Supplement Material Fig. S2, a continuous wave with a 532 nm
448 wavelength was generated by laser (YFA-SF-1064-50-CW, Precilaser), and injected into a single-
449 mode optical fiber with a length of 3m to shape the beam profile. To match the polarization state
450 of the spatial light modulator (SLM; X13139-09, Hamamatsu), a zero-order half-wave plate
451 (HWP) and a polarizing beam splitter (PBS) were inserted to produce the polarization along the
452 SLM and control the power of the light. In the case of scattering media (ZnO with 400 μm thickness
453 or ground glass with 600 grit), the beam was focused by an objective lens (20 \times /0.4NA, Olympus).
454 For MMF (SR-opt-8039, 2 m length, $\text{\O}105 \mu\text{m}$, 0.22NA, Andor) and glucose aqueous solution,
455 the beam was focused through an objective lens with a larger numerical aperture (50 \times /0.6NA, TU
456 Plan ELWD, Nikon). Then, speckles were collected by an objective lens (10 \times /0.3NA, UPlanFL
457 N, Olympus) and recorded by a charge-coupled device (CCD; Prosilica GT1910, AVT with pixel
458 size of 5.5 μm and 8-bits monochrome mode) for further subsequent information extraction. For
459 dynamic hidden objects classification in NLOS scenes, the diffuse reflector consisted of a single
460 layer of Scotch tape and a mirror, and the SLM operated in amplitude-only mode by placing an
461 HWP with its fast axis at 22.5 $^\circ$ (see Supplement Material Fig. S3 for details). The transport mean
462 free path is $\sim 110 \mu\text{m}$ and $\sim 40 \mu\text{m}$ for ground glass and ZnO sample, respectively.

463 *Dynamic environment for MMF*: A MMF with a length of 2m was wound into coils with a 10
464 cm diameter. To mimic environmental disturbances, an inhomogeneous stress was imposed on
465 such coils by a motorized rotator with a constant velocity of 20°/s and two loose clamps, where
466 friction was randomly applied to the MMF. The collected speckles were randomly attenuated in
467 time to verify the compatibility of SURE with intensity modulation for optical communications.
468 When nonlinear effects of light propagation through the fiber can be ignored, the time-sequence
469 random attenuation of the collected data is equivalent to directly attenuating the power of light.

470 *Glucose solution preparation*: The glucose stock solution was prepared with a concentration of
471 0.305 mol/L (D-glucose: 549 mg, deionized water: 10 mL). In the experiment, 3 mL of water and
472 0.08 mL of the stock solution were added into the cuvette to obtain an 8 mmol/L glucose aqueous
473 solution corresponding to the average level of a healthy people. Subsequently, 0.04 mL of the stock
474 solution was continued to be added to obtain a 12 mmol/L corresponding to the average level of
475 patient with hyperglycemia. Noted that the cuvette was wrapped with two layers of scotch tape to
476 simulate thin scattering media. The rear surface of the cuvette had an extra layer of egg membrane
477 as a thick backscattering layer.

478 *Dynamic NLOS scene*: The NLOS scene was mimicked by a diffuse reflector composed of a
479 processed Scotch tape and a scratched silver mirror. The quasi-Gaussian light illuminated the
480 diffuse reflector generating forward and backward scattering, where backward scattered photons
481 were projected onto the detector and the forward scattered photons entered the NLOS region to
482 illuminate the dynamic hidden objects. These hidden objects were created by a SLM operating in
483 amplitude-only mode realized by a HWP and a PBS where phases 0 and π correspond to light on
484 and off, respectively. They were randomly loaded onto different active regions of the SLM and
485 then scattered the forward scattered photons onto the diffuse reflector to undergo a second
486 scattering process. The first backward and second forward scattered photons simultaneously
487 entered the detector to be captured.

488 5.2 Data Acquisition

489 In the task of speckle image clustering, the MNIST dataset was used as the modulation phase map,
490 where the size of each image was interpolated from 28×28 to 400×400 using bicubic interpolation.
491 The recorded speckles had 256×256 pixels with 8-bit grayscale. All MNIST data was loaded into
492 the SLM one by one, and 70,000 speckle images were acquired to build the dataset. For the

493 experiment of information transport based on dynamic MMF, the DIV2K dataset was adopted to
494 modulate the phase with a total of 800 images, each appearing 100 times. The size of each phase
495 map was 256×256 pixels, and the corresponding speckles had 256×256 pixels (8-bit). Here, 256
496 classes were randomly selected to build a dataset with 25,600 speckles. For noninvasive glucose
497 monitoring, the acquisition interval of each image was 5 seconds with $1,024 \times 1,024$ pixels (16-bit).
498 Since the change in speckle arising from the change in glucose concentration was slight compared
499 with the influence of the environmental disturbance, we grouped 25 continuous frames of speckles
500 to construct one video, which can facilitate SURE for information extraction from speckles. For
501 dynamic hidden objects classification under NLOS scenes, we used triangles, squares, and circles,
502 as well as their corresponding hollow patterns to mimic 6 classes of objects. These objects
503 occupied 700×700 pixel area and were randomly imposed onto an 800×800 pixel area of the SLM.
504 Each object had 6,000 random coordinates and a total of 36,000 speckle images with 256×256
505 pixels were generated to establish the dataset. The pixel size of SLM is $12.5 \mu\text{m}$, and thus the
506 physical sizes of object with 400×400 pixels is $5 \times 5 \text{ mm}^2$. The pixel size of CCD is $5.6 \mu\text{m}$ such
507 that the physical sizes of speckle with 256×256 pixels is $1.434 \times 1.434 \text{ mm}^2$. All demonstrative
508 experiment only input speckle without any other information.

509 *5.3 SCAN Implementation*

510 *Structure:* SCAN utilizes invariant information to maximize mutual information for clustering. Its
511 basic structure comprises a convolutional neural network (CNN) for feature extraction, a fully
512 connected (FC) layer for clustering and an overclustering module to enhance feature extraction. In
513 the clustering procedure, speckles are cropped at the center to single-channel 64×64 pixels and
514 perform random transformations. The pre-processing speckle images are then fed into the CNN
515 consisting of 3×3 convolution, Batch Normalization, Leaky ReLU and average pooling, to extract
516 feature maps with 1024 channels and 8×8 pixels. Subsequently, the feature maps are flattened and
517 fed into the FC layer (clustering or overclustering module) to yield the probability for each batch
518 over the relevant clusters. The input neurons of the FC layer are $1024 \times 8 \times 8$ and the output neurons
519 are matched to the number of classes. To enhance the stability of the training process, multiple
520 clustering modules with disparate initialization processes are employed to collaboratively fine-
521 tune the parameters of SCAN (see Supplement Material Fig. S1 for details).

522 *Training:* The PyTorch framework was used to build the SCAN model, and its training and
523 evaluation were implemented on a server (Intel Xeon Gold 6248 CPU, Tesla V100 PCIe 32GB
524 GPU, CUDA10.2). Before training, the auxiliary dataset is created by random transformations of
525 the original dataset, such as scaling, skewing, rotating and flipping, to facilitate the CNN in
526 capturing the invariant information from speckles. During training, the CNN has two inputs that
527 are sampled from the original and auxiliary datasets, and are separately fed into the CNN to
528 generate the corresponding feature maps for the subsequent FC layer. When the original and
529 transformed data are grouped into the same class, it indicates that the CNN has extracted crucial
530 invariant features from speckles and the FC layers can accurately classify them. To further improve
531 the effectiveness of feature extraction, SCAN incorporates an overclustering module which is also
532 an FC structure but has a significantly larger number of output classes than the preset cluster
533 number. The aim of the overclustering module is still to group the original and transformed data
534 into the same class. Since more classes are introduced, the classification requires more precise and
535 sufficient features to be extracted by the CNN. The training process alternately utilizes the
536 overclustering and clustering modules in each epoch. The best clustering module (lowest loss) is
537 selected to serve as the model output.

538 In SCAN, we select the invariant information clustering (IIC)-Loss function as loss function,
539 which is defined as⁶⁴⁰,

$$540 \quad L = -\sum_{jh} \{P_{jh} \cdot [\ln P_{jh} - \ln(P_j P_h)]\} \quad (1)$$

$$541 \quad P_{jh} = \frac{1}{n} \sum_{i=1}^n [P_i(y = j) \cdot P_i(y' = h)] \quad (2)$$

542 where $P_i \in [0,1]^C$ is the probability of network output corresponding to each cluster of the i -th sample
543 pairs in each batch (batch size is n) and C is the total number of clusters. Since there are two ways
544 to sample a data pair, (x, x') or (x', x) , we only considered the symmetry problem with
545 $\mathbf{P} = (\mathbf{P} + \mathbf{P}^T) / 2$ where \mathbf{P} is a matrix with elements of P_{jh} . The marginal probabilities $P_j = P(y = j)$
546 and $P_h = P(y' = h)$ can be calculated by summing the rows and columns of \mathbf{P} . The CNN module,
547 clustering module, and over-clustering module are weight-sharing in each stage. To improve the
548 robustness of SCAN, we parallelly trained multiple clustering modules and the loss of all clustering
549 modules was averaged to serve as the final loss. The Adam optimizer was run for 40 epochs with
550 the initial learning rate of 10^{-4} .

551 *Evaluation:* Due to the absence of the ground truth, when one speckle image is input, the neural
552 network can merely predict the corresponding probability of each clustering group without the
553 actual meanings of the class. This leads to the results of SCAN being disorderly distributed in the
554 confusion matrix, such that it is difficult to determine the correspondence between SCAN’s output
555 numbers and the actual label numbers. To address this, SCAN utilized linear assignment to find
556 the best one-to-one permutation mapping of the predictions of the testing dataset. Here, we let \mathbf{M}
557 be a $C \times C$ matrix with columns representing the predicted clusters and rows representing the true
558 clusters of the sample. In the linear assignment method, \mathbf{X} is assumed to be a Boolean matrix of
559 $C \times C$. If the j -th predicted label corresponds to the h -th true label, then the value of X_{jh} is 1. Once
560 the optimal mapping is achieved, the corresponding \mathbf{X} satisfies the maximization of $\sum_{jh} M_{jh} X_{jh}$. The
561 “linear_sum_assignment” function in the SciPy library was employed to complete the linear
562 assignment and return the best mapping. To quantitatively evaluate the clustering performance,
563 the ground truth was introduced in this step without being presented in the training process. The
564 accuracy of clustering was defined as the ratio of true positives to total samples, which is used to
565 evaluate the performance of SURE. The inference time per speckle is ~ 10 ms.

566 *Comparison:* Although conceptually inspired by IIC⁵⁶, our SCAN framework is structurally and
567 functionally distinct. SCAN adopts a lightweight 6-layer CNN, designed to balance representation
568 capability with computational efficiency, in contrast to the deeper and heavier architectures
569 typically used in IIC. For data augmentation, SCAN applies a broader set of geometric
570 transformations—including scaling, skewing, rotation, and affine operations—tailored to the
571 statistical nature of speckle patterns, whereas IIC relies on semantic-preserving transformations
572 suited for natural images. During training, SCAN alternates between clustering and overclustering
573 objectives with adjustable output dimensions, enhancing feature abstraction and avoiding mode
574 collapse. Importantly, SCAN is physically grounded in the context of light scattering and
575 wavefront modulation, enabling robust application to complex optical environments beyond the
576 scope of IIC.

577 5.4 SHACK Implementation

578 SHACK is an agglomeration clustering algorithm that creates a hierarchical nested clustering
579 tree by calculating the similarity among all speckles (see Supplement Material Fig. S1 for details).
580 Each sample is treated as a unit in SHACK, and two units with the highest similarity are grouped

581 together. As a result, the total number of units decreases by one. This process is repeated until the
582 number of clusters matches the ground truth number of clusters. Concretely, for each step of
583 hierarchical clustering, speckle images are paired in all possible combinations. The paired images
584 are treated as a new unit and the variance for all pixel values within the unit is calculated (initially,
585 the variance of each sample is set to 0). The difference in variance between after and before pairing
586 is defined as the cost function. Traverse all possible pairs and select the pair with the smallest cost
587 function as the result of the current clustering step. The "AgglomerativeClustering" class of Scikit-
588 Learn library was used to build SHACK with the Euclidean distance for measuring the similarity.
589 The speckle images were down-sampled to 64×64 pixels, then flattened and fed into SHACK for
590 training. Similarly, the linear assignment was employed to find the best one-to-one permutation
591 mapping. SHACK implement in whole dataset and can be integrated with other regression model
592 to achieve inference with millisecond scale.

593 5.5 *Mutual Information Estimation*

594 We note that analytically characterizing invariant information is challenging due to the
595 nonlinear and stochastic nature of coherent light propagation through scattering media. A feasible
596 statistical method is to calculate the mutual information of speckles and the original information
597 labels to obtain the map of the mutual information distribution. To estimate the mutual information
598 between continuous features and target variables, we adopt a non-parametric approach based on
599 k-nearest neighbors distance estimation. Specifically, mutual information $I(x_i; y) = H(x_i) + H(y) -$
600 $H(x_i; y)$ can be calculated by the entropy $H(x_i)$ of i -th pixel of all speckles, the entropy $H(y)$ of all
601 label information and the joint entropy i -th speckle pixel and label. Each entropy term is estimated
602 using the average distance to the k -th nearest neighbor in the respective space. The entropy of each
603 variable is approximated using digamma functions of the number of neighbors within these
604 distances. This method enables mutual information estimation without assuming specific data
605 distributions, making it well-suited for evaluating the dependency between high-dimensional
606 continuous variables such as speckle features and class labels. The estimation of mutual
607 information can be achieved by calling the `mutual_info_regression` function in Scikit-Learn
608 library. The quantitative results are shown in Supplement Material Fig. S11.

609

610 *Disclosures*

611 The authors declare that there are no financial interests, commercial affiliations, or other potential
612 conflicts of interest that could have influenced the objectivity of this research or the writing of this
613 paper.

614 *Code and Data, and Availability*

615 The archived version of the code described in this manuscript can be freely accessed through
616 GitHub at <https://github.com/weirufan/SURE>. Data are available from the corresponding author
617 upon request.

618 *Supplemental Documentation*

619 See Supplementary Material for supporting content.

620 *Acknowledgments*

621 This work was supported by the National Natural Science Foundation of China (Grant No.
622 11934011, 12074339, 62075194, U21A6006, 62202418, U21B2004), the National Key Research
623 and Development Program of China (Grant No. 2019YFA0308100, 2023YFB2806000,
624 2022YFA1204700), the Strategic Priority Research Program of Chinese Academy of Sciences
625 (Grant No. XDB28000000), the Leading Innovation and Entrepreneurship Team in Zhejiang
626 Province (Grant No. 2020R01001), the Open Program of the State Key Laboratory of Advanced
627 Optical Communication Systems and Networks at Shanghai Jiao Tong University (Grant No.
628 2023GZKF024), the Fundamental Research Funds for the Central Universities, the Information
629 Technology Center and State Key Lab of CAD&CG at Zhejiang University, the Zhejiang
630 Provincial Key Laboratory of Information Processing, Communication and Networking (IPCAN),
631 and the National Institutes of Health (NIH) (R01GM127696, R01GM152633, R21GM142107, and
632 R21CA269099).

633 *References*

- 634 1. S. Rotter and S. Gigan, “Light fields in complex media: Mesoscopic scattering meets wave control,”
635 *Rev. Mod. Phys.* **89**, 015005 (2017).
- 636 2. R. Savo, R. Pierrat, U. Najar, et al, “Observation of mean path length invariance in light-scattering
637 media,” *Science* **358**, 765–768 (2017).

- 638 3. B. Redding, M. A. Choma, and H. Cao, "Speckle-free laser imaging using random laser
639 illumination," *Nat. Photonics* **6**, 355–359 (2012).
- 640 4. V. Bianco, P. Memmolo, M. Leo, et al, "Strategies for reducing speckle noise in digital holography,"
641 *Light. Sci. & Appl.* **7**, 48 (2018).
- 642 5. O. V. Michailovich and A. Tannenbaum, "Despeckling of medical ultrasound images," *IEEE Trans.*
643 *on Ultrason. Ferroelectr. Freq. Control.* **53**, 64–78 (2006).
- 644 6. E. Mudry, K. Belkebir, J. Girard, et al, "Structured illumination microscopy using unknown speckle
645 patterns," *Nat. Photonics* **6**, 312–315 (2012).
- 646 7. Y. Choi, M. Kim, C. Park, et al, "Wide-field super-resolution optical fluctuation imaging through
647 dynamic near-field speckle illumination," *Nano Lett.* **22**, 2194–2201 (2022).
- 648 8. K. W. Gossage, T. S. Tkaczyk, J. J. Rodriguez, and J. K. Barton, "Texture analysis of optical
649 coherence tomography images: feasibility for tissue classification," *J. Biomed. Opt.* **8**, 570–575
650 (2003).
- 651 9. B. Redding, S. F. Liew, R. Sarma, and H. Cao, "Compact spectrometer based on a disordered
652 photonic chip," *Nat. Photonics* **7**, 746–751 (2013).
- 653 10. N. Antipa, G. Kuo, R. Heckel, et al, "Diffusercam: lensless single-exposure 3d imaging," *Optica* **5**,
654 1–9 (2018).
- 655 11. J. Bertolotti, E. G. Van Putten, C. Blum, et al, "Non-invasive imaging through opaque scattering
656 layers," *Nature* **491**, 232–234 (2012).
- 657 12. O. Katz, P. Heidmann, M. Fink, and S. Gigan, "Non-invasive single-shot imaging through scattering
658 layers and around corners via speckle correlations," *Nat. Photonics* **8**, 784–790 (2014).
- 659 13. S. M. Popoff, G. Lerosey, R. Carminati, et al, "Measuring the transmission matrix in optics: An
660 approach to the study and control of light propagation in disordered media," *Phys. Rev. Lett.* **104**,
661 100601 (2010).
- 662 14. W. Fan, Z. Chen, V. V. Yakovlev, and J. Pu, "High-fidelity image reconstruction through multimode
663 fiber via polarization-enhanced parametric speckle imaging," *Laser & Photonics Rev.* **15**, 2000376
664 (2021).
- 665 15. V. B. Silva, D. Andrade De Jesus, S. Klein, et al, "Signal-carrying speckle in optical coherence
666 tomography: a methodological review on biomedical applications," *J. Biomed. Opt.* **27**, 030901
667 (2022).
- 668 16. H. Hugonnet, Y. W. Kim, M. Lee, et al, "Multiscale label-free volumetric holographic histopathology
669 of thick-tissue slides with subcellular resolution," *Adv. Photonics* **3**, 026004 (2021).
- 670 17. T. Yeminy, and O. Katz, "Guidestar-free image-guided wavefront shaping," *Sci. Adv.* **7**, eabf5364
671 (2021).

- 672 18. Z. Yu, H. Li, T. Zhong, et al, “Wavefront shaping: A versatile tool to conquer multiple scattering in
673 multidisciplinary fields,” *The innovation* **3**, 100292 (2022).
- 674 19. O. Haim, J. Boger-Lombard, and O. Katz, “Image-guided computational holographic wavefront
675 shaping,” *Nat. Photonics* **19**, 44–53 (2025).
- 676 20. Y. Li, Y. Xue, and L. Tian, “Deep speckle correlation: a deep learning approach toward scalable
677 imaging through scattering media,” *Optica* **5**, 1181–1190 (2018).
- 678 21. B. Rahmani, D. Loterie, G. Konstantinou, et al, “Multimode optical fiber transmission with a deep
679 learning network,” *Light. Sci. & Appl.* **7**, 69 (2018).
- 680 22. S. Li, M. Deng, J. Lee, et al, “Imaging through glass diffusers using densely connected convolutional
681 networks,” *Optica* **5**, 803–813 (2018).
- 682 23. N. Borhani, E. Kakkava, C. Moser, and D. Psaltis, “Learning to see through multimode fibers,”
683 *Optica* **5**, 960–966 (2018).
- 684 24. T. Wang, M. M. Sohoni, L. G. Wright, et al, “Image sensing with multilayer nonlinear optical neural
685 networks,” *Nat. Photonics* **17**, 408–415 (2023).
- 686 25. D. A. Boas and A. K. Dunn, “Laser speckle contrast imaging in biomedical optics,” *J. Biomed. Opt.*
687 **15**, 011109–011109 (2010).
- 688 26. Y. Wang, D. C. Louie, J. Cai, et al, “Deep learning enhances polarization speckle for in vivo skin
689 cancer detection,” *Opt. & Laser Technol.* **140**, 107006 (2021).
- 690 27. A. Sezer and H. B. Sezer, “Deep convolutional neural network-based automatic classification of
691 neonatal hip ultrasound images: A novel data augmentation approach with speckle noise reduction,”
692 *Ultrasound Med. & Biol.* **46**, 735–749 (2020).
- 693 28. L. Gong, Q. Zhao, H. Zhang, et al, “Optical orbital-angular-momentum-multiplexed data transmission
694 under high scattering,” *Light. Sci. & Appl.* **8**, 27 (2019).
- 695 29. Z. Zhu, M. Janasik, A. Fyffe, et al, “Compensation-free high-dimensional free-space optical
696 communication using turbulence-resilient vector beams,” *Nat. Commun.* **12**, 1666 (2021).
- 697 30. Y. Luo, Y. Zhao, J. Li, et al, “Computational imaging without a computer: Seeing through random
698 diffusers at the speed of light,” *eLight* **2**, 4 (2022).
- 699 31. Y. LeCun, Y. Bengio, and G. Hinton, “Deep learning,” *Nature* **521**, 436–444 (2015).
- 700 32. T. Poggio, A. Banburski, and Q. Liao, “Theoretical issues in deep networks,” *Proc. National Acad.*
701 *Sci.* **117**, 30039–30045 (2020).
- 702 33. F. Zhuang, Z. Qi, K. Duan, et al, “A comprehensive survey on transfer learning,” *Proc. IEEE* **109**,
703 43–76 (2020).
- 704 34. J. E. Van Engelen and H. H. Hoos, “A survey on semi-supervised learning,” *Mach. Learn.* **109**, 373–
705 440 (2020).

- 706 35. B. Rahmani, D. Loterie, E. Kakkava, et al, "Actor neural networks for the robust control of partially
707 measured nonlinear systems showcased for image propagation through diffuse media," *Nat. Mach.*
708 *Intell.* **2**, 403–410 (2020).
- 709 36. M. Krenn, J. Handsteiner, M. Fink, et al, "Twisted light transmission over 143 km," *Proc. National*
710 *Acad. Sci.* **113**, 13648–13653 (2016).
- 711 37. F. Wang, C. Wang, M. Chen, et al, "Far-field super-resolution ghost imaging with a deep neural
712 network constraint," *Light. Sci. & Appl.* **11**, 1 (2022).
- 713 38. A. Goy, G. Rughoobur, S. Li, et al, "High-resolution limited-angle phase tomography of dense
714 layered objects using deep neural networks," *Proc. National Acad. Sci.* **116**, 19848–19856 (2019).
- 715 39. N. Bender, M. Sun, H. Yilmaz, et al, "Circumventing the optical diffraction limit with customized
716 speckles," *Optica* **8**, 122–129 (2021).
- 717 40. O. Sagi and L. Rokach, "Ensemble learning: A survey," *WIREs Data Min. Knowl. Discov.* **8**, e1249
718 (2018).
- 719 41. Z.-H. Zhou, "Senseble learning," in *Machine Learning*, (Springer Singapore, Singapore, 2021), pp.
720 181–210.
- 721 42. R. Bilous, R. Donnelly, and I. Idris, *Handbook of diabetes* (John Wiley & Sons, Oxford, 2021).
- 722 43. M.-S. Steiner, A. Duerkop, and O. S. Wolfbeis, "Optical methods for sensing glucose," *Chem. Soc.*
723 *Rev.* **40**, 4805–4839 (2011).
- 724 44. V. V. Tuchin, *Handbook of optical sensing of glucose in biological fluids and tissues* (CRC press,
725 Boca Raton, 2008).
- 726 45. N. Ozana, N. Arbel, Y. Beiderman, et al, "Improved noncontact optical sensor for detection of
727 glucose concentration and indication of dehydration level," *Biomed. Opt. Express* **5**, 1926–1940
728 (2014).
- 729 [46.](#) N. Ozana, R. Talman, A. Shemer, et al, "Remote photonic sensing of glucose concentration via
730 analysis of time varied speckle patterns," *Adv. Mater. Lett.* **9**, 624–628 (2018).
- 731 [47.](#) [A. Sdobnov, G. Piavchenko, A. Bykov, et al, "Advances in dynamic light scattering imaging of blood](#)
732 [flow," Laser Photonics Rev. 18, 2300494 \(2024\).](#)
- 733 [46.48.](#) [E. Zherebtsov, A. Sdobnov, O. Sieryi, et al, "Enhancing transcranial blood flow visualization with](#)
734 [dynamic light scattering technologies: advances in quantitative analysis," Laser Photonics Rev. 19,](#)
735 [2401016 \(2025\)](#)
- 736 [47.49.](#) D. Pal, S. Agadarov, Y. Beiderman, et al, "Non-invasive blood glucose sensing by machine
737 learning of optic fiber-based speckle pattern variation," *J. Biomed. Opt.* **27**, 097001–097001 (2022).

738 [48-50](#). M. Gusev, L. Poposka, G. Spasevski, et al, “Noninvasive glucose measurement using machine
739 learning and neural network methods and correlation with heart rate variability,” *J. Sensors* **2020**,
740 9628281 (2020).

741 [51](#). D. Pal, A. Kumar, N. Avraham, et al, “Noninvasive blood glucose sensing by secondary speckle
742 pattern artificial intelligence analyses,” *J. Biomed. Opt.* **28**, 087001–087001 (2023).

743 [52](#). [M. Monemian, M. Irajpour, and H. Rabbani](#), “[A review on texture-based methods for anomaly
744 detection in retinal optical coherence tomography images.](#)” *Optik* **288**, 171165 (2023).

745 [49-53](#). [A. El-Baz, Mo. Ghazal, and J. S. Suri](#), *Handbook of texture analysis: AI-based medical imaging
746 applications* (CRC Press, Boca Raton, 2024).

747 [50-54](#). L. Tang, S. J. Chang, C.-J. Chen, and J.-T. Liu, “Non-invasive blood glucose monitoring
748 technology: A review,” *Sensors* **20**, 6925 (2020).

749 [54-55](#). G. Euliss and C. Sorensen, “Dynamic light scattering studies of concentration fluctuations in
750 aqueous t-butyl alcohol solutions,” *J. Chem. Phys.* **80**, 4767–4773 (1984).

751 [52-56](#). K. Yoshizaki, O. Urakawa, and K. Adachi, “Dielectric study of concentration fluctuation in
752 solutions of polystyrene,” *Macromolecules* **36**, 2349–2354 (2003).

753 [53-57](#). X.-L. Wu, D. Pine, and P. Dixon, “Enhanced concentration fluctuations in polymer solutions under
754 shear flow,” *Phys. Rev. Lett.* **66**, 2408 (1991).

755 [54-58](#). J. Hecht, *City of light: The story of fiber optics* (Oxford University Press, USA, New York, 2004).

756 [55-59](#). N. Bozinovic, Y. Yue, Y. Ren, et al, “Terabit-scale orbital angular momentum mode division
757 multiplexing in fibers,” *Science* **340**, 1545–1548 (2013).

758 [56-60](#). A. Willner, ed., *Optical fiber telecommunications* (Academic Press, 2019).

759 [57-61](#). Z. Xue, T. Zhou, Z. Xu, et al, “Fully forward mode training for optical neural networks,” *Nature*
760 **632**, 280–286 (2024).

761 [58-62](#). T. Wang and P. Isola, “Understanding contrastive representation learning through alignment and
762 uniformity on the hypersphere,” in *International conference on machine learning*, (PMLR, 2020), pp.
763 9929–9939.

764 [63](#). A. Momeni, B. Rahmani, M. Malléjac, et al, “Backpropagation-free training of deep physical neural
765 networks,” *Science* **382**, 1297–1303 (2023).

766 [59](#). [X. Ji, J. F. Henriques, and A. Vedaldi](#), “[Invariant information clustering for unsupervised image
767 classification and segmentation.](#)” in *Proceedings of the IEEE/CVF international conference on
768 computer vision*, 9865–9874 (2019).

769 [64](#).

770 ~~60. X. Ji, J. F. Henriques, and A. Vedaldi, "Invariant information clustering for unsupervised image~~
771 ~~classification and segmentation," in *Proceedings of the IEEE/CVF international conference on computer*~~
772 ~~*vision*, 9865–9874 (2019).~~

773

774

775 Biographies and photographs for the other authors are not available.

776

777

778 **Caption List**

779

780 **Fig. 1** The overall concept of speckle clustering for image recognition and the data workflow.

781 **Fig. 2** Clustering results of different complex media.

782 **Fig. 3** Experimental schematics and results of SURE-based high-sensitive noninvasive glucose
783 monitoring.

784 **Fig. 4** SURE-based high-throughput dynamic MMF information transmission.

785 **Table 1** Comparison between different speckle processing modalities.

786 **Table 2** Quantitative comparison between different algorithms.